Journal of Power Sources 244 (2013) 488–493

Contents lists available at SciVerse ScienceDirect

Journal of Power Sources

journal homepage: www.elsevier.com/locate/jpowsour

A study of Pt_xCo_y alloy nanoparticles as cathode catalysts for lithium-air batteries with improved catalytic activity

Dawei Su [a,*], Hyun-Soo Kim [b], Woo-Seong Kim [c], Guoxiu Wang [a,*,1]

[a] Centre for Clean Energy Technology, School of Chemistry and Forensic Science, University of Technology, Sydney, NSW 2000, Australia
[b] Battery Research Centre, Korea Electrotechnology Research Institute, Changwon 641-120, Republic of Korea
[c] Daejung Energy Materials Co., Ltd, Iksan 570-977, Republic of Korea

HIGHLIGHTS

- A series of Pt_xCo_y alloy nanoparticles as catalysts in lithium-air batteries was prepared.
- They significantly increased the specific capacity of lithium-air batteries.
- Especially, $PtCo_2$ demonstrated 3040 mAh/g discharge capacity (three times over bare carbon).
- The charge and discharge over-potential was decreased after the addition of Pt_xCo_y catalysts.

GRAPHICAL ABSTRACT

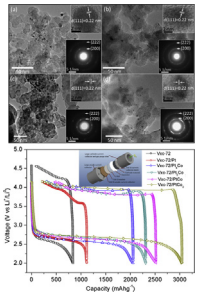

ARTICLE INFO

Article history:
Received 19 September 2012
Received in revised form
6 November 2012
Accepted 9 November 2012
Available online 19 November 2012

Keywords:
Pt–Co alloy nanoparticles
Catalyst
Electrochemical performance
Lithium-air batteries

ABSTRACT

A series of Pt_xCo_y (x:y = 4, 2, 1, and 0.5) alloy nanoparticles deposited on Vulcan XC-72 carbon was prepared through a chemical reduction method. The structures and morphologies of the as-prepared nanoparticles were characterized by X-ray diffraction, field emission scanning electron microscopy and transmission electron microscopy, which revealed the formation of Pt–Co alloys during the co-reduction process. Pt_xCo_y alloy nanoparticles were applied as catalysts in lithium-air batteries. Through electrochemical testing, we found that the Pt based alloy nanocatalysts significantly increased the specific capacity of lithium-air batteries and the increase of Co content in Pt_xCo_y alloy nanoparticles further enhanced the catalytic activity. This result illustrated that Pt_xCo_y alloy nanoparticles could be used as an efficient catalyst material for lithium-air batteries with the feature of much reduced cost, but drastically increased catalytic activity.

1. Introduction

Li ion batteries are currently the most advanced power sources for portable electronic devices and have potential to power future electric vehicles (EVs) and hybrid electric vehicles (HEVs). However, the energy density of present lithium ion batteries is limited by available electrode materials, in particular, cathode materials [1–8]. $LiCoO_2$ cathode material can only deliver a practical capacity of 140 mAh/g [9–11] and $LiNi_{1/3}Mn_{1/3}Co_{1/3}O_2$ cathode has a specific capacity of about 200 mAh/g [12–14]. The increase of the capacity of cathode materials for a few times higher is a formidable challenge that requires a fundamental breakthrough. Lithium-air batteries based on the ($anode^{Li\ metal}$|electrolyte|$cathode^{oxygen}$) configuration have a much higher energy density than that of lithium ion batteries because the cathode active material (oxygen) can be persistently supplied from the environment [15–17].

* Corresponding authors. Tel.: +61 2 95148244; fax: +61 2 95141460.
E-mail addresses: Dawei.Su@student.uts.edu.au (D. Su), Guoxiu.Wang@uts.edu.au (G. Wang).
[1] Tel.: +61 2 95141741; fax: +61 2 2 95141460.

0378-7753/$ – see front matter © 2012 Elsevier B.V. All rights reserved.
http://dx.doi.org/10.1016/j.jpowsour.2012.11.024

Recently, lithium-air batteries have attracted worldwide attention as a promising power source for large-scale applications such as electric vehicles and stationary energy storage [18–24].

Although the air-cathode in lithium-air batteries can provide a 5–10 fold higher capacity than that of intercalation electrodes, the development of lithium-air batteries faces a number of problems such as low round-trip efficiency, short cyclability, the consumption of electrolyte, and a lower capacity than that of theoretical value [25–27]. The nature of the catalyst plays a key role on the overall performance of lithium-air batteries. In the past few years, many catalysts have been developed for lithium-air batteries. P.G. Bruce's group has systematically investigated transition metal oxide catalysts [28]. They found that the addition of Fe_2O_3 catalyst on porous carbon cathode electrode generated the highest initial capacity. They also discovered that Fe_3O_4, CuO and $CoFe_2O_4$ have the best capacity retention, while Co_3O_4 catalyst can generate the lowest charging voltage (4 V). Additionally, they found that α-MnO_2 nanowires give the highest charge storage capacity [22]. Other studies have investigated the effects of the active functional platinum and gold nanoparticle catalysts for the reaction kinetics of the oxygen reduction reaction (ORR) and the oxygen evolution reaction (OER) [29]. The results showed that Pt and Au can greatly influence the discharge and charge voltages. Au is the most active for ORR and Pt is the most active for OER. The PtAu alloy catalysts demonstrated the highest round-trip efficiency [30]. However, the PtAu bifunctional catalyst does not provide high specific capacity. Furthermore, Pt and Au are all expensive, and the world's supply is limited. Therefore, it is necessary to develop new catalysts with reduced costs.

In this study, we synthesised a series of Pt_xCo_y (x:y = 0, 4, 2, 1, and 0.5) alloy nanoparticles as catalysts for lithium-air batteries. The partial replacement of Pt with Co can not only reduce the costs of catalyst materials, but also maintain or even enhance catalytic activity in lithium-air batteries.

2. Experimental

2.1. Preparation of Pt_xCo_y catalyst nanoparticles

Nanosize Pt_xCo_y (x:y = 4, 2, 1, and 0.5) alloy catalysts on a carbon matrix were prepared by a chemical reduction method. In a typical synthesis process, $H_2PtCl_6 \cdot 6H_2O$ (Aldrich, 99.9%) and $CoCl_2 \cdot 6H_2O$ (Aldrich, 99.9%) was dissolved in 200 ml de-ionized water with appropriate Pt:Co ratios to prepare nanosized Pt_xCo_y alloy catalysts. Then, Vulcan XC-72 carbon was added to the solution to obtain a weight ratio of Pt_xCo_y:C = 20:80. In order to achieve homogeneous dispersion, the solution was ultrasonicated for about 2 h

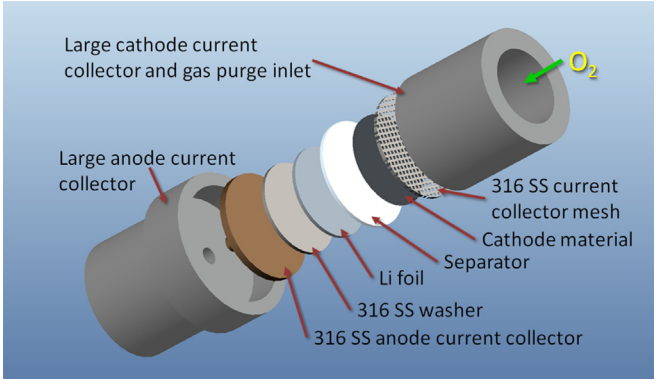

Fig. 1. Schematic diagram of the lithium-air test cell.

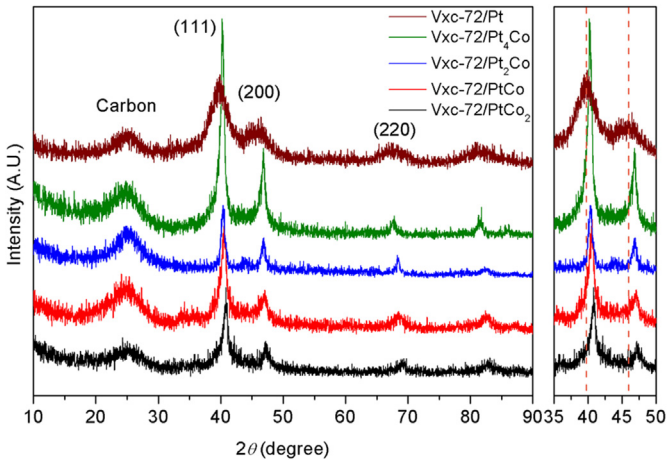

Fig. 2. X-ray diffraction patterns of Pt_xCo_y catalyst nanoparticles deposited on Vulcan XC-72 carbon matrix.

(Brandson Ultrasonifier, 35% amplitude). The mixture was heated to 140 °C in a three-neck round-bottom flask under flowing argon gas in an oil bath, in which 15 ml aqueous solution of superfluous $NaBH_4$ (60 mg, Aldrich, 99.9%) was added into the mixture for reduction. The dispersion was stirred and refluxed continuously for 1 h and then cooled down to room temperature. The reduction product was retrieved by washing 3–4 times with ethanol. Finally, the black powder was dried at 50 °C in a vacuum oven overnight. As compared the standard commercial Pt/Vulcan XC-72 carbon sample (Aldrich, 98%) was also used.

2.2. Material characterization

The crystal structure and phase of the as-prepared Pt_xCo_y alloy catalyst deposited on Vulcan XC-72 carbon were characterized by X-ray diffraction (XRD, Siemens D5000) using Cu K_α radiation with 2θ ranging from 10° to 90° at a scanning step 0.01°/min. The morphology was analysed by high-resolution field emission scanning electron microscopes (FESEM, Zeiss Supra 55VP). The microscope was operated at a working distance of 2 mm with an acceleration voltage of 20 kV and in-lens detector was used for the imaging. The elemental composition of Pt_xCo_y alloy nanoparticles was examined by X-ray energy dispersive spectroscopy (EDS, Oxford EDS system). The crystal structure of Pt_xCo_y alloy nanoparticles was further characterized by transmission electron microscopy (TEM) and high-resolution transmission electron microscopy (HRTEM, JEOL JEM-2011). Selected area electron diffraction (SAED) patterns were recorded by a Gatan CCD camera in a digital format. The Inductively Coupled Plasma-Mass Spectrometry (ICP-MS, Agilent 7500 Series) was used to quantify the elemental composition.

2.3. Assembling of lithium-air cells and electrochemical testing

A Swagelog type cell was used to investigate the catalytic activity of Pt_xCo_y nanoparticles as catalysts in lithium-air cells. Fig. 1

Table 1
Average crystallite sizes and lattice parameters determined by XRD.

Sample	Crystallite size (nm)	Lattice parameter (Å)
Pt_4Co	8.5	3.916
Pt_2Co	6.1	3.863
PtCo	6.0	3.845
$PtCo_2$	5.4	3.834

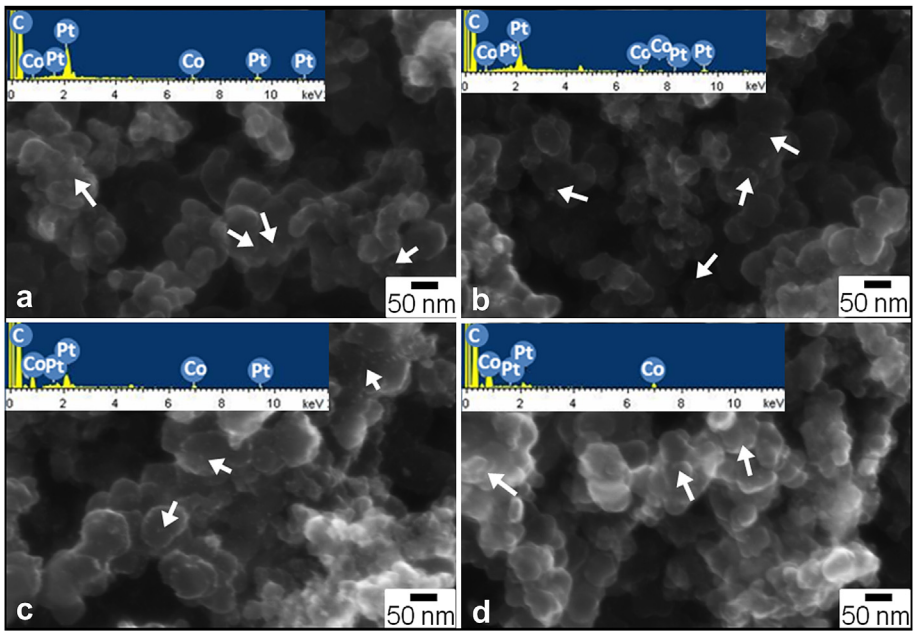

Fig. 3. SEM images of Pt_xCo_y/Vulcan XC-72 carbon, (a) Pt_4Co, (b) Pt_2Co, (c) PtCo, and (d) $PtCo_2$.

shows a schematic diagram of the test cell, which consisted of a stainless steel cylinder plunger to support a Li foil anode (3 mm × ø 15 mm) and a special stainless steel tube to allow oxygen access to the back side of the cathode. A glass microfibre filter (Whatman, ø 21 mm) separator was used, soaked in 1 M $LiClO_4$ in a propylene carbonate (PC): 1,2-dimethoxyethane (DME) (1:2 v/v) electrolyte, prepared from $LiClO_4$, PC, and DME from Aldrich (all <30 ppm H_2O). The cathode was formed by casting a mixture of cathode catalysts (90 wt. %), PTFE (10 wt. %, Aldrich) and 2-propanol (Aldrich) on the stainless steel mesh. All cathode carbon loadings were within 1 ± 0.15 mg (0.65 ± 0.1 mg/cm^2$_{electrode}$). The cathode was placed onto the separator and a thin open 316 stainless steel mesh was placed on top to act as a current collector. The entire cell was gastight except for the stainless steel mesh window exposed the porous cathode to the O_2 atmosphere. The assembling of the test cells was carried out in an argon atmosphere in a glove box (Unilab, MBRAUN, Germany), in which water and oxygen levels were controlled to be less than 0.1 ppm. We used a low voltage limit at 2.0 V_{Li} and upper limit 4.6 V_{Li} for the pure Vulcan carbon electrode, 4.2 V_{Li} for the Pt_xCo_y/Vulcan XC-72 carbon electrodes and standard commercial Pt/Vulcan XC-72 carbon electrode. The cells were charged and discharged at a constant current of 100 mA/g.

3. Results and discussion

Fig. 2 shows the X-ray diffraction patterns of Pt_xCo_y/Vulcan XC-72 carbon, indicating that Pt and Co atoms form a solid-solution, in which all sharp diffraction peaks are in agreement with the previously reported face-centre cubic (fcc) phase of platinum (PDF card No. 01-1194) [31]. The diffraction peaks at 40°, 47°, and 68° can be indexed to Pt (1 1 1), (2 0 0) and (2 2 0), respectively. The broad diffraction peak at about 25° indicates the appearance of amorphous Vulcan XC-72 carbon. We estimated Pt_xCo_y catalysts' average size from the broadening Full Width of single peak (at ~40°) in the patterns according to the Scherrer formula which was used by reference [32]

$$\text{Crystallite size} = K \times \lambda / \text{FW}(S) \times \cos(\theta)$$

where θ is the peak position, λ is the wavelength of the radiation and K is the shape factor of the average crystallite (0.5 at here), and $\text{FW}(S)^D = \text{FWHM}^D - \text{FW}(I)^D$, where FWHM is the Full Width at Half Maximum and FW(I) is calculated from the current FWHM curve and D is called the deconvolution parameter and was set as 2.0. The calculated average crystallite sizes of all the catalysts are all around 5–8 nm as listed in the Table 1.

In further from the magnified image between the 35 and 50° it can be clearly seen that the major diffraction peaks of Pt_xCo_y (x:y = 4, 2, 1, and 0.5) catalysts are gradually shifted to higher angle along with the increase of Co content compared with the pure Pt sample. This signifies a contraction of the lattice according to the Bragg formula due to the incorporation of Co into the fcc crystal structure of Pt. And we computed approximate lattice constants from the locations of low-angle peaks with known Miller indices ((111), (200), and (220)). It showed the tendency that the lattice parameters of the Pt_xCo_y alloy catalysts decrease with increasing Co content as listed values in the Table 1. No characteristic diffraction peaks of metallic Co or cobalt oxides were detected, suggesting that the oxidation of Co can be effectively prevented by the use of flowing argon gas during the reduction process.

Table 2
EDX spectrum of Pt_xCo_y/Vulcan XC-72 carbon matrix.

Element	Pt_4Co		Pt_2Co		PtCo		$PtCo_2$	
	Wt.%	At. %	Wt.%	At. %	Wt.%	At. %	Wt.%	At. %
C K	80.69		80.17		81.41		81.05	
Co L	1.38	20.12	2.7	34.18	4.46	50.93	7.02	66.15
Pt M	17.93	79.88	17.13	65.82	14.13	49.07	11.93	33.85

Table 3
ICP-MS quantified the elemental composition of the Pt_xCo_y alloy

Samples	ng/ml		nmol/ml		Atomic ratio (Co:Pt)
	Co	Pt	Co	Pt	
Pt_4Co	74	898.7	1.256367	4.608718	0.272607
Pt_2Co	105.8	647.2	1.796265	3.318974	0.541211
PtCo	117.6	352.64	1.996604	1.80841	1.104066
$PtCo_2$	173.1	297.04	2.938879	1.523282	1.929307

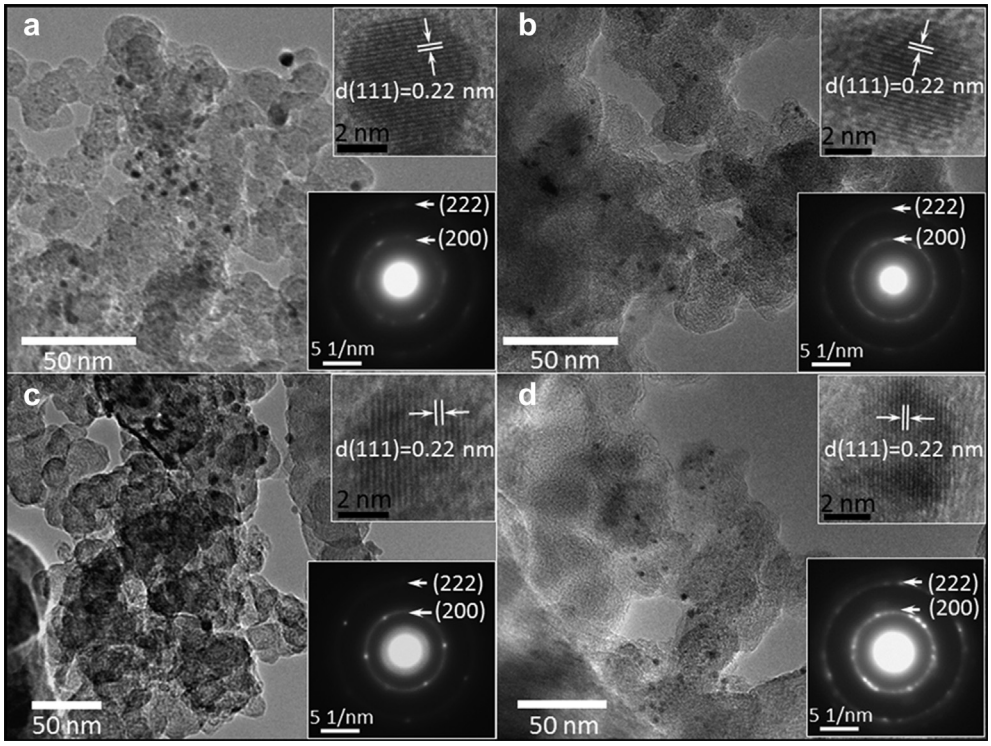

Fig. 4. TEM images of Pt_xCo_y/Vulcan XC-72 carbon, (a) Pt_4Co, (b) Pt_2Co, (c) PtCo, and (d) $PtCo_2$. The insets are the corresponding select area diffraction patterns and the right up corner inset of (d) is the lattice resolved high-resolution TEM image of a single $PtCo_2$ nanoparticle.

Fig. 3 shows the FESEM images of Pt_xCo_y/Vulcan XC-72 carbon catalyst materials. All four samples exhibit similar morphology, consisting of primary carbon nanoparticles with a size in the range of 50–100 nm, in which the uniform distribution of the catalysts nanoparticles can be seen and pointed out by the arrows. The elemental compositions were quantitatively determined by EDS spectra analysis (inset of each subfigure of Fig. 3). The weight ratios of C:Pt_xCo_y for all samples are approximately 80:20, which confirms 20 wt% catalyst loading in the carbon matrix (as shown in Table 2). The atomic ratios of Pt:Co in Pt_xCo_y nanoparticles have been determined to be very close to the nominal ratios. We also used the Inductively Coupled Plasma-Mass Spectrometry (ICP-MS) to quantify the elemental composition. The results confirm the atomic ratio of Pt and Co in each sample as shown in Table 3.

The crystal structure and morphology of Pt_xCo_y/carbon catalysts were further analysed by TEM and HRTEM analyses (as shown in Fig. 4). In general, Pt_xCo_y nanoparticles have a superfine particle size in the range of a few nanometres and uniformly embedded in carbon matrix. All the corresponding SAED patterns (shown as the insets in Fig. 4) clearly show the two main crystal plains ((200) and (222) with 0.19 and 0.11 nm d-spacings, respectively) of the Pt_xCo_y (x:y = 0, 4, 2, 1, and 0.5) nanoparticles, and the additional diffuse rings correspond to amorphous Vulcan XC-72 carbon. The lattice resolved HRTEM images of typical free stand Pt_xCo_y nanoparticles presenting the (111) crystal plane (with 0.22 nm d-spacing) revealing their good crystallinity (insets of Fig. 4). It also can be seen that they have less than 10 nm particle size, which is consistent with the results deduced from XRD.

The electrochemical performance of Pt_xCo_y/carbon catalyst materials was tested through galvanostatical charge and discharge. Fig. 5(a) and (b) show the voltage–capacity profiles of bare Vulcan XC-72 carbon cathode and $PtCo_2$/carbon cathode in the first five cycles, respectively. For the bare Vulcan XC-72 carbon electrode, the potentials decent rapidly to the plateau at about 2.7 V during the first discharge process and then decrease continuously to 2.0 V. The discharge capacity is about 965 mAh/g. After 5 cycles, the discharge capacity degraded to 376 mAh/g. On the contrary, the specific capacity and cyclability of $PtCo_2$/carbon catalyst material have been significantly improved. As shown in Fig. 5(b), the $PtCo_2$/carbon cathode delivered a specific capacity of 2578 mAh/g in the first cycle and reached the maximum of 3040 mAh/g in the second cycle, which is more than three times over the bare carbon catalyst. After 5 cycles, it retained a capacity of 2074 mAh/g with much enhanced capacity retention, comparing with the bare Vulcan XC-72 carbon. Fig. 6 compares the discharge and charge curves of bare carbon, standard commercial Pt/Vulcan XC-72 carbon and all Pt_xCo_y/carbon catalyst materials in the second cycle. By analysing the profiles of discharge and charge curves, we found that the bare carbon electrode delivered an average discharge voltage of 2.57 V and a charge voltage of 4.5 V; while, the Pt_xCo_y/carbon catalysts show a higher average discharge voltage of 2.73 V and much lower charge voltage of 3.94 V. The charging potential of Pt_xCo_y/carbon catalysts is slightly lower than that of previously reported MnO_2 and Co_3O_4 catalysts (4.0 V) [21,28,29]. From Fig. 6, we can determine that the Pt_xCo_y/carbon electrodes have an over-potential of 1.21 V, which is significantly lower than that of the bare carbon electrode (1.93 V). In addition it can be observed that the standard commercial Pt/Vulcan XC-72 electrode have 1197 mAh/g discharge capacity at second cycle, while the Pt_xCo_y/Vulcan XC-72 (x:y = 4, 2, 1, and 0.5) electrodes all have much higher capacity than this value. Furthermore, the specific capacities increase positively with Co content in Pt_xCo_y nanoparticles, indicating the improved catalytic activity towards ORR and OER reactions in lithium-air cells.

Alloys of noble metal have been evaluated for bi-functional oxygen electrode activity, and they were shown to perform better than the pure metals or metal oxides [33–35]. The previous investigations have identified that PtAu nanoparticles have bi-functional catalytic activity and exhibited lower over-potential. A mechanism of surface Au and Pt atoms serving for ORR and OER kinetics has also been proposed [30,36]. However, the PtAu/carbon

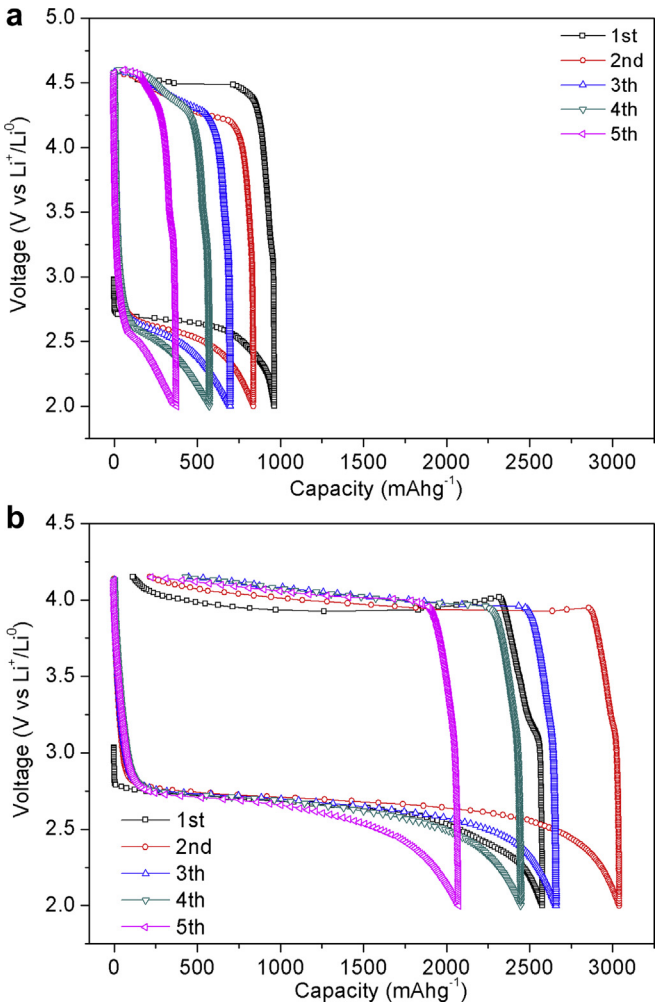

Fig. 5. Charge/discharge of Vulcan XC-72 carbon electrode (a) and $PtCo_2$/Vulcan XC-72 carbon electrode; (b) (rate: 100 mA/g).

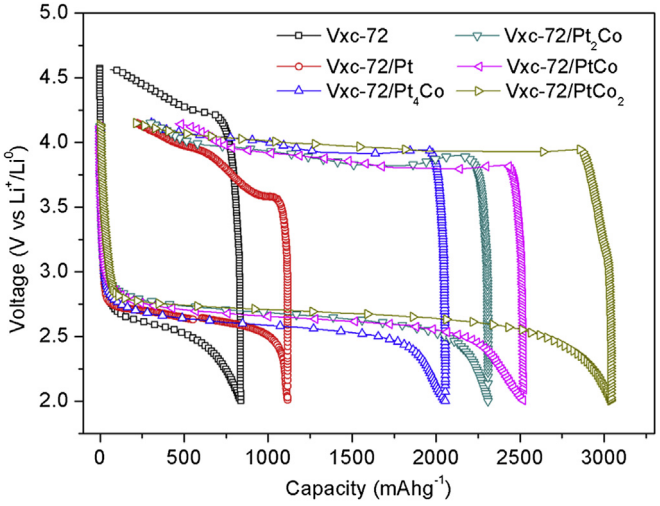

Fig. 6. Voltage–capacity curves of Pt_xCo_y(x:y = 4, 2, 1, and 0.5)/Vulcan XC-72 carbon electrodes (second cycle) compared with Vulcan XC-72 and Pt/Vulcan XC-72 in lithium-air cells.

catalyst (with 40 wt% loading of PtAu nanoparticles) showed a relatively low specific capacity of about 1200 mAh/g in the first cycle. Comparing to PtAu catalyst, our $PtCo_2$/carbon catalyst (with 20wt% loading of $PtCo_2$ nanoparticles) demonstrated much higher capacity (3100 mAh/g).

Experiments indicated that only the outer monolayer of such catalyst is involved in the reaction [37]. In detail, the utilization and efficiency of current OER catalysts can be improved through increasing surface area and electronic conductivity [38]. The presence of a different metallic atom in the vicinity of a Pt atom can increase Pt electron density which enhance its ability to adsorb and transfer electrons to oxygenated species. Thus, the presence of Co sites in the subsurface can contribute favourably to making Pt a better centre for electron transfer and adsorption of oxygenated species to improve the OER efficiency at here [39]. Furthermore, the surface chemistry, atomic and electronic structures of Pt alloy model surfaces have been changed which can also contribute to the higher ORR activity [40,41]. Density functional theory (DFT) studies of Norskov et al. [41] and Mavrikakis et al. [42] have shown that the enhanced ORR activity of Pt_3M (M = Co, Fe, Ni) surfaces with the Pt-skin can be attributed to weakening metal–oxygen bond strength relative to pure Pt. This reduced surface reactivity of the Pt-skin structure results from lowered Pt valence band centre relative to the Fermi level [43], which is induced both by shortened surface Pt–Pt bond distance constrained by transition metals in the second layer beneath the surface and by ligand effect [42,44,45]. More M in the vicinity of Pt atoms, more surface Pt segregation will be presented which can be proposed the improvement of ORR activity. Therefore, the enhanced electrocatalytic activity of the Pt_xCo_y (x:y = 4,2,1,0.5) alloy catalysts could be attributed to that amount of lower electronegativity Co atoms sitting in the vicinity of Pt atoms increase electron density of Pt and weaken the strength of the metal–oxygen bond, corresponding to the improvement of the OER efficiency and ORR activity respectively. Along with Co content increase in the vicinity of Pt atoms, the increase of surface Pt electron density and segregation will be presented which can be proposed the enhancement of OER and ORR activity both. Therefore $PtCo_2$ shows the best performance of the electrocatalytic activity. Fig. 7 shows the cycling performance of Pt_xCo_y/carbon and bare carbon cathode in lithium-air cells. In general, Pt_xCo_y/carbon catalysts exhibited better cyclability than that of bare carbon catalyst. The $PtCo_2$/cabon sample demonstrated the highest capacity among all catalyst materials.

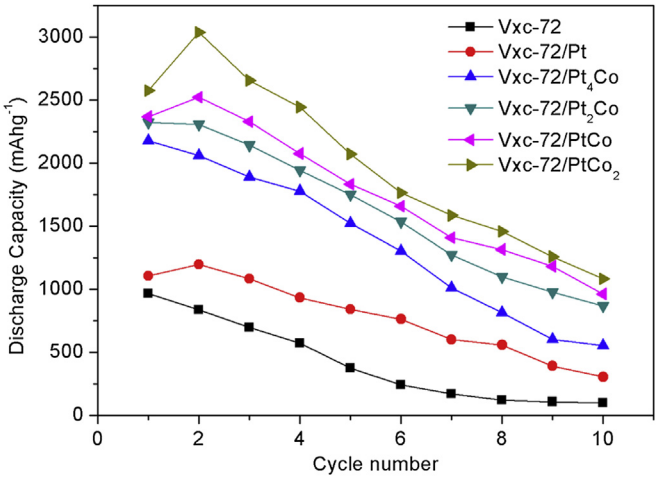

Fig. 7. The relationship between specific discharge capacity and cycle number for Pt_xCo_y (x:y = 4, 2, 1, and 0.5)/Vulcan XC-72 carbon electrodes compared with Vulcan XC-72 and Pt/ Vulcan XC-72 in lithium-air cells.

4. Conclusion

Pt_xCo_y (x:y = 4, 2, 1, and 0.5) alloy nanoparticles were synthesised and applied as cathode catalysts in lithium-air cells. TEM and HRTEM characterisation confirmed that Pt–Co alloy nanoparticles are embedded in the carbon matrix with particle sizes in the range of a few nanometres. Electrochemical testing results indicated that the presence of Co in Pt–Co alloy nanoparticles significantly enhanced the electrocatalytic activity in lithium-air cells. In particular, the $PtCo_2$ nanoparticle catalyst demonstrated a high discharge capacity of 3040 mAh/g, which is more than three times over the bare carbon. This contributes to its potential as an efficient catalyst material for lithium-air batteries.

Acknowledgements

This research is financially supported by the Australian Research Council (ARC), through the Discovery Project (DP1093855) and ARC Future Fellowship Project (FT110100800). We thank David Bishop for assistance on ICP-MS analysis.

References

[1] J.M. Tarascon, M.J. Armand, Nature 414 (2001) 359.
[2] K. Mizushima, P.C. Jones, P.J. Wiseman, J.B. Goodenough, Mater. Res. Bull. 15 (1980) 783.
[3] T. Nagaura, K. Tozawa, Prog. Batteries Sol. Cells 9 (1990) 209.
[4] J.M. Tarascon, M. Armand, Nature 414 (2001) 359.
[5] A.K. Padhi, K.S. Nanjundaswamy, J.B. Goodenough, J. Electrochem. Soc. 144 (1997) 1108.
[6] A.S. Andersson, J.O. Thomas, J. Power Sources 97 (2001) 498.
[7] O. Toprakci, L.W. Ji, Z. Lin, H.A.K. Toprakci, X.W. Zhang, J. Power Sources 196 (2011) 7692.
[8] A. Yamada, S. Chung, K.J. Hinokuma, J. Electrochem. Soc. 148 (2001) A224.
[9] T. Ohzuku, A. Ueda, J. Electrochem. Soc. 139 (1992) 2091.
[10] A.R. Armstrong, P.G. Bruce, Nature 381 (1996) 499.
[11] F. Jiao, K.M. Shaju, P.G. Bruce, Angew. Chem. Int. Ed. 44 (2005) 6550.
[12] T. Ohzuku, Y. Makimura, Chem. Lett. 7 (2001) 642.
[13] K.M. Shaju, G.V. Subba Rao, B.V.R. Chowdari, Electrochim. Acta 48 (2002) 145.
[14] N. Yabuuchi, T. Ohzuku, J. Power Sources 119 (2003) 171.
[15] D. Linden (Ed.), Handbook of Batteries, third ed,, McGraw-Hill, New York, 2001.
[16] A. Kraytsberg, Y. Ein-Eli, J. Power Sources 196 (2011) 886.
[17] C.J. Patrissi, C.R. Schumacher, S.P. Tucker, J.H. Fontaine, D.W. Atwater, C.M. Deschenes, Eleventh Electrochemical Power Sources R&D Symposium, Baltimore, MD, (2009) July 13–16.
[18] G. Girishkumar, B. McCloskey, A.C. Luntz, S. Swanson, W. Wilcke, J. Phys. Chem. Lett. 1 (2010) 2193.
[19] J. Read, J. Electrochem. Soc. 149 (2002) A1190.
[20] H. Cheng, K. Scott, J. Power Sources 195 (2010) 1370.
[21] T. Ogasawara, A. Débart, M. Holzapfel, P. Novák, P.G. Bruce, J. Am. Chem. Soc. 128 (2006) 1390.
[22] S.S. Zhang, D. Foster, J. Read, J. Power Sources 195 (2010) 1235.
[23] J. Read, K. Mutolo, M. Ervin, W. Behl, J. Wolfenstine, A. Driedger, D. Foster, J. Electrochem. Soc. 150 (2003) A1351.
[24] J.S. Hummelshøj, J. Blomqvist, S. Datta, T. Vegge, J. Rossmeisl, K.S. Thygesen, A.C. Luntz, K.W. Jacobsen, J.K. Norskøv, J. Chem. Phys. 132 (2010) 071101.
[25] Y. Wang, H. Zhou, J. Power Sources 195 (1) (2010) 358.
[26] B. Kumar, J. Kumar, R. Leese, J.P. Fellner, S.J. Rodrigues, K.M. Abraham, J. Electrochem. Soc. 157 (1) (2010) A50.
[27] Z. Deng, Z.H. Fu, Z. Wei, T. Huang, A.S. Yu, J. Electrochem. Soc. 157 (2010) A362.
[28] A. Débart, J.L. Bao, G. Armstrong, P.G. Bruce, J. Power Sources 174 (2007) 1177.
[29] A. Débart, A.J. Paterson, J.L. Bao, P.G. Bruce, Angew. Chem. Int. Ed. 47 (2008) 4521.
[30] Y.C. Lu, H.A. Gasteiger, M.C. Parent, V. Chiloyan, S.H. Yang, Electrochem. Solid-State Lett. 13 (6) (2010) A69.
[31] Y.C. Lu, Z.C. Xu, H.A. Gasteiger, S. Chen, H.S. Kimberly, S.H. Yang, J. Am. Chem. Soc. 132 (2010) 12170.
[32] T. Reier, M. Oezaslan, P. Strasser, ACS Catal. 2 (2012) 1765.
[33] Y. Gorlin, T.F. Jaramillo, J. Am. Chem. Soc. 132 (2010) 13612.
[34] S. Koh, P. Strasser, J. Am. Chem. Soc. 129 (2007) 12624.
[35] Y.J. Zhang, C. Wang, N.F. Wan, Z.Q. Mao, Int. J. Hydrogen Energy 32 (2007) 400.
[36] H.M. Wu, D. Wexler, H.K. Liu, O. Savadogo, J. Ahn, G.X. Wang, Mater. Chem. Phys. 124 (2010) 841.
[37] S. Fierro, T. Nagel, H. Baltruschat, C. Comninellis, Electrochem. Commun 9 (2007) 1969.
[38] K.C. Neyerlin, G. Bugosh, R. Forgie, Z. Liu, P. Strasser, J. Electrochem. Soc. 156 (2009) B363.
[39] J.M. Seminario, L.A. Agapito, L. Yan, P.B. Balbuena, Chem. Phys. Lett. 410 (2005) 275.
[40] V.R. Stamenkovic, B. Fowler, B.S. Mun, G.F. Wang, P.N. Ross, C.A. Lucas, N.M. Markovic, Science 315 (2007) 493.
[41] J.K. Norskov, J. Rossmeisl, A. Logadottir, L. Lindqvist, J.R. Kitchin, T. Bligaard, H.J. Jonsson, Phys. Chem. B 108 (2004) 17886.
[42] Y. Xu, A.V. Ruban, M. Mavrikakis, J. Am. Chem. Soc. 126 (2004) 4717.
[43] B.S. Mun, M. Watanabe, M. Rossi, V. Stamenkovic, N.M. Markovic, P.N. Ross, J. Chem. Phys. 123 (2005) 204717.
[44] J.R. Kitchin, J.K. Norskov, M.A. Barteau, J.G. Chen, Phys. Rev. Lett. 93 (2004) 156801.
[45] S. Mukerjee, S. Srinivasan, M.P. Soriaga, J. McBreen, J. Electrochem. Soc. 142 (1995) 1409.